Discrete time crystal in an open optomechanical system

Dongni Chen,[1,2,3] Zhenyang Peng,[1,2,4] Jiahui Li,[5,6] Stefano Chesi,[6,7,*] and Yingdan Wang[1,2,†]

[1]*Key Laboratory of Frontiers in Theoretical Physics, Institute of Theoretical Physics, Chinese Academy of Sciences, Beijing 100190, China*

[2]*School of Physical Sciences, University of Chinese Academy of Sciences, Beijing 100049, China*

[3]*Department of Physics, Korea University, Seoul 02841, South Korea*

[4]*Wilczek Quantum Center, School of Physics and Astronomy, Shanghai Jiao Tong University, Shanghai 200240, China*

[5]*School of Future Technology, Henan University, Zhengzhou 450046, China*

[6]*Beijing Computational Science Research Center, Beijing 100193, People's Republic of China*

[7]*Department of Physics, Beijing Normal University, Beijing 100875, People's Republic of China*

(Received 18 August 2023; accepted 9 January 2024; published 31 January 2024)

The spontaneous breaking of time translation symmetry in periodically driven Floquet systems can lead to a discrete time crystal. Here we study the occurrence of such dynamical phase in a driven-dissipative optomechanical system with two membranes in the middle. We find that, under certain conditions, the system can be mapped to an open Dicke model and realizes a superradiant-type phase transition. Furthermore, applying a suitable periodically modulated drive, the system dynamics exhibits a robust subharmonic oscillation persistent in the thermodynamic limit.

DOI: 10.1103/PhysRevResearch.6.013130

I. INTRODUCTION

As an analog to spatial crystals, Wilczek first proposed the idea of *time crystals* in 2012 [1]. Soon, it was pointed out that a system where continuous time invariance is spontaneously broken would naturally radiate energy into the environment, which conflicts with the principle of energy conservation [2]. Indeed, formal no-go theorems have shown that time crystals cannot exist in equilibrium [3,4]. On the other hand, broken time translational invariance is still allowed under nonequilibrium conditions, where the concept of *discrete time crystals* (DTCs) has been proposed [5–7]. A DTC is realized in a periodically driven system, with Hamiltonian satisfying $H(t) = H(t+T)$, and breaks discrete time translational symmetry, i.e., the period of the dynamics is a multiple of the driving period T [8]. In a genuine DTC phase such spontaneously generated subharmonic response should be robust against parameter variations and persist to arbitrarily long times in the thermodynamic limit [7–9]. Experimentally, DTCs have been explored with trapped ions [10], vacancy-based quantum simulators [11], superfluid helium-3 [12], spin NMR systems [13,14], and a driven atom-cavity system [15]. Besides, various generalizations have been proposed theoretically, such as the realizations of a DTC in the Dicke model [16–19], finite chains of Rydberg atoms [20], in the presence of quasiperiodic spatial modulations [21], or topological DTCs [22].

While most DTC realizations and proposals are based on an interacting spin model, in the past decades optomechanical systems (where light interacts with motional degrees of freedom) have become one of the most promising platforms for exploring macroscopic quantum-mechanical behaviors and quantum information processing. This is due to their high coherence, the presence of an intrinsic nonlinear coupling, and the ability to couple in a versatile way to other quantum systems [23,24]. A large variety of quantum engineering protocols have been proposed in optomechanics [24]. Among them, of special relevance here is a "membrane in the middle" setup realizing a Dicke-type phase transition [25]. In that system, the mechanical mode and two cavity modes are mapped to the bosonic mode and collective spin of the Dicke model, respectively. However, cavity dissipation in optomechanical systems is normally much larger than the dissipation of the membranes. Hence the mapping leads to a Dicke model where dissipation acts predominantly on the collective spin, unlike typical quantum-optics realization (where cavity dissipation dominates [26–28]). Furthermore, applying Schwinger's spin-boson mapping leads to a collective decay of total angular momentum, which differs from the more usual collective decay (see, e.g., Ref. [29]) or individual spin decoherence [28,30,31].

Inspired by the above proposal, we consider here an alternative "two membranes in the middle" setup, which can realize a more typical Dicke-type phase transition. A main difference is that, in our model, light-matter degrees of freedom are not swapped by the mapping: the cavity and mechanical modes of the optomechanical setup correspond to the cavity mode and the collective spin of the Dicke model, respectively. Therefore, due to the much smaller decay rate of the membranes compared to cavity decay, the conservation of the atomic angular momentum (in the Dicke model) is a much better approximation. We show that the Dicke phase transition

*stefano.chesi@csrc.ac.cn

†yingdan.wang@itp.ac.cn

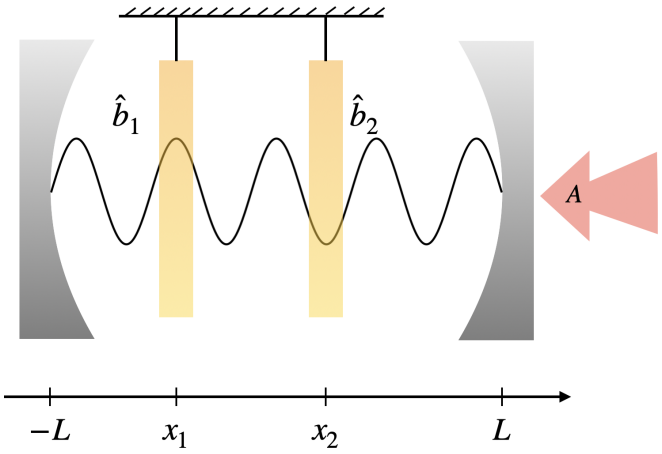

FIG. 1. Schematics of the system, with two membranes inside a driven Fabry-Pérot cavity. The positions $x_{1,2}$ of the mirrors are discussed in Appendix A.

can be simulated in this optomechanical system with realistic parameters. Furthermore, we analyze the realization of a DTC phase, which for the Dicke model has been recently discussed in Refs. [16,17]. Unfortunately, the simple approach of pulsing on/off the effective coupling is not directly applicable to our system, due to the specific features of the optomechanical system and the mapping. Thus we develop an alternative sequence of control pulses which can achieve an equivalent result.

The outline of our paper is as follows. In Sec. II we introduced our "two membranes in a cavity" model and its mapping to the Dicke model. In Sec. III we study the phase transition and phase diagram of this model. The validity of various approximations invoked in the mapping are also checked. In Sec. IV the pulse sequence to realize the DTC is presented. We also provide discussions on various issues such as the choice of flipping time, the robustness of the DTC phase, the fate of the DTC in the deep quantum regime, and the influence of mechanical damping. Finally, we summarize our work in Sec. V. Some technical details are given in Appendixes A and B.

II. EFFECTIVE DICKE MODEL

The optomechanical system we consider is formed by two mechanical membranes inside a driven optical cavity, schematically shown in Fig. 1. The two membranes are located at antinodes of the cavity field, such that only second-order optomechanical couplings are significant. The Hamiltonian reads (setting $\hbar = 1$)

$$\hat{H} = \omega_c \hat{a}^\dagger \hat{a} + \omega_1 \hat{b}_1^\dagger \hat{b}_1 + \omega_2 \hat{b}_2^\dagger \hat{b}_2 + \hat{H}_I + \hat{H}_D, \tag{1}$$

where $\omega_{1,2}$ (ω_c) is the frequency of the relevant mechanical modes (cavity mode) with annihilation operators $\hat{b}_{1,2}$ ($\hat{a}$). The interaction ($\hat{H}_I$) and drive ($\hat{H}_D$) Hamiltonians are given by

$$\hat{H}_I = g\hat{a}^\dagger \hat{a}(\hat{b}_1^\dagger + \hat{b}_1)^2 - g\hat{a}^\dagger \hat{a}(\hat{b}_2 + \hat{b}_2^\dagger)^2 + J(\hat{b}_1^\dagger + \hat{b}_1 - \hat{b}_2^\dagger - \hat{b}_2)^2, \tag{2}$$

$$\hat{H}_D = A(\hat{a}\, e^{i\omega_D t} + \hat{a}^\dagger e^{-i\omega_D t}). \tag{3}$$

Here the second-order optomechanical couplings of the cavity with the two membranes are assumed to have opposite values ($g_1 = -g_2 = g$). The feasibility of this condition is discussed in detail in Appendix A), while the case $g_1 \neq g_2$ will be considered in Sec. IV. J is the direct coupling between the two membranes which can be implemented through a coupling overhang [32–36]. In $\hat{H}_D$, the parameters ω_D and A are the frequency and the amplitude of the drive, where $A = \sqrt{2P_L\kappa/\omega_c}$ depends on the power of the drive P_L and the decay rate of the cavity field κ. For the moment, we will neglect the small damping of the mechanical modes. Effects of a finite decay rate γ will be discussed in Sec. IV E.

We now show that, under appropriate conditions, the above optomechanical system becomes equivalent to the Dicke model, describing the interaction of a cavity mode with an ensemble of identical two-level systems. At strong drive, the optical cavity mode $\hat{a}$ can be decomposed as $\hat{a} = (\alpha + \hat{d}')e^{-i\omega_D t}$, where $\hat{d}'$ represents the quantum fluctuations and α is the large classical amplitude of the driven cavity mode:

$$\alpha = \frac{A}{i\kappa - \Delta} \equiv |\alpha| \exp[i\theta], \tag{4}$$

with $\Delta = \omega_c - \omega_D$ the detuning, which we choose positive. The interaction $\hat{H}_I$ leads to modified mechanical frequencies, $\tilde{\omega}_{1(2)} = \omega_{1(2)} + 2J \pm 2g|\alpha|^2$. Considering a working point with equal effective frequencies:

$$\omega_1 + 2J + 2g|\alpha|^2 = \omega_2 + 2J - 2g|\alpha|^2 \equiv \omega_m, \tag{5}$$

we can derive the following effective Hamiltonian in the rotating frame $U = e^{-i\omega_D t\hat{a}^\dagger \hat{a} - i\omega_m t(\hat{b}_1^\dagger \hat{b}_1 + \hat{b}_2^\dagger \hat{b}_2)}$:

$$\hat{H}_{\text{eff}} = \Delta \hat{d}^\dagger \hat{d} + 2g|\alpha|(\hat{d} + \hat{d}^\dagger)(\hat{b}_1^\dagger \hat{b}_1 - \hat{b}_2^\dagger \hat{b}_2) - 2J(\hat{b}_1 \hat{b}_2^\dagger + \hat{b}_1^\dagger \hat{b}_2), \tag{6}$$

where we have defined $\hat{d} \equiv \hat{d}' \exp[-i\theta]$. Here, taking the rotating wave approximation (RWA), high frequency oscillating terms were neglected, leading to an effective Hamiltonian where the number of total phonons is conserved, i.e., $[\hat{N}, \hat{H}_{\text{eff}}] = 0$ ($\hat{N} = \hat{b}_1^\dagger \hat{b}_1 + \hat{b}_2^\dagger \hat{b}_2$). We see that, applying the Schwinger's representation to Eq. (6), $\hat{J}_z = -(\hat{b}_1^\dagger \hat{b}_2 + \hat{b}_2^\dagger \hat{b}_1)/2$, $\hat{J}_x = (\hat{b}_1^\dagger \hat{b}_1 - \hat{b}_2^\dagger \hat{b}_2)/2$, the mechanical degrees of freedom can be written in terms of spin variables:

$$\hat{H}_{\text{eff}} = \Delta \hat{d}^\dagger \hat{d} + 4J\hat{J}_z + 4g|\alpha|(\hat{d} + \hat{d}^\dagger)\hat{J}_x. \tag{7}$$

Thus the system is mapped onto a Dicke model with a dissipative cavity. In a standard notation [26,28]

$$H_{\text{DM}} = \omega_0 \hat{c}^\dagger c + \omega_z \hat{J}_z + \frac{2\lambda}{\sqrt{N_a}}(\hat{c} + \hat{c}^\dagger)\hat{J}_x, \tag{8}$$

where $\hat{c}$ is the cavity mode and $\hat{J}_{z/x} = \frac{1}{2}\sum_{i=1}^{N_a} \hat{\sigma}_{z/x}^i$ are collective atomic operators, with $\hat{\sigma}_\alpha$ the Pauli matrices. The mapping yields $\omega_0 = \Delta$ and $\omega_z = 4J$ for the cavity and atomic frequencies, respectively. The coupling strength is given by $\lambda = 2g|\alpha|\sqrt{N_a}$, where the size N_a of the atomic ensemble can be identified with the number $\hat{N}$ of mechanical excitations.

It is worth pointing out that another Dicke model realization in optomechanics has been proposed, considering a membrane in the middle setup [25]. In that case, however, the roles of optical and mechanical degrees of freedom are

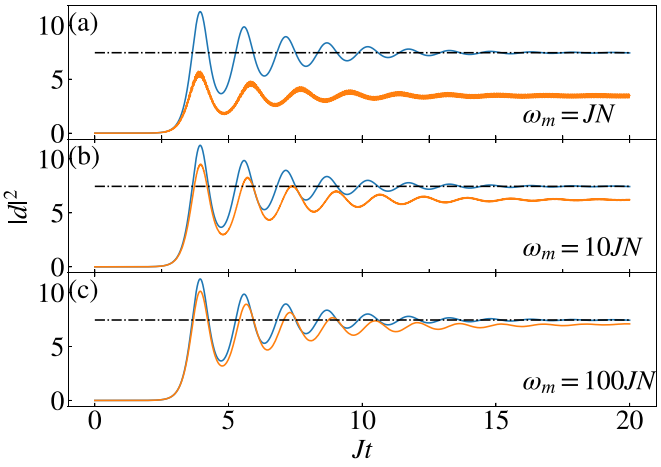

FIG. 2. Validity of the effective model. In each panel, the lower (orange) curve is obtained computing $|a-\alpha|^2$ from the mean-field equations of the full model and the upper (blue) curve is obtained from the effective Hamiltonian. The black dot-dashed lines refer to the mean-field steady state of the effective model, given by Eq. (12). The three panels are computed for $N = 200$ and $\omega_m/NJ = 1, 10, 100$ (from top to bottom). Other parameters are $A/J = 2000$, $\Delta/J = 20$, $\kappa/J = 10$, $b_1(0) = b_2(0) = 10$, and $g = 1.2g_c$. We compute g_c as in Eq. (11), while ω_1, ω_2 are decided by Eq. (5).

switched, as the Dicke model cavity is mapped to a single mechanical membrane. Conversely, the spin ensemble is mapped to a pair of cavity modes. Therefore, in such a realization the total angular momentum of the atomic ensemble decays to zero quickly, due the large damping of the optomechanical cavities. In contrast, in our system the role of the spin ensemble is played by the phonon modes, whose damping can be 10^5–10^6 times smaller than κ [23,37]. Thus the Dicke model is implemented in a more standard scenario.

In the rest of the paper, we will discuss the quantum phase transition and a protocol to realize a discrete time crystal based on our setup with two membranes. The validity of the effective model Eq. (6) can be tested through the mean-field approximation of the equations of motion:

$$\begin{aligned} i\frac{d}{dt}b_1 &= 2g|\alpha|(d+d^*)b_1 - 2Jb_2, \\ i\frac{d}{dt}b_2 &= -2g|\alpha|(d+d^*)b_2 - 2Jb_1, \\ i\frac{d}{dt}d &= \Delta d + 2g|\alpha|(b_1^* b_1 - b_2^* b_2) - i\kappa d, \end{aligned} \tag{9}$$

where $\langle\hat{b}_1\rangle = b_1$, $\langle\hat{b}_2\rangle = b_2$, and $\langle\hat{d}\rangle = d$. Here, quantum fluctuations are neglected and the factorization of expectation values is imposed, $\langle(\hat{d}+\hat{d}^\dagger)\hat{b}_i\rangle \to \langle(\hat{d}+\hat{d}^\dagger)\rangle\langle\hat{b}_i\rangle$, $\langle\hat{b}_i^\dagger\hat{b}_i\rangle \to \langle\hat{b}_i^\dagger\rangle\langle\hat{b}_i\rangle$ (with $i = 1, 2$). Analogous equations can be derived from the full model, Eq. (1). A comparison between numerical results is shown in Fig. 2, showing good agreement when ω_m is increased. This is because the two main approximations, linearization and RWA, require a sufficiently large α and $\omega_m \gg J(b_i^2 + b_i^{\dagger 2})$, $g|\alpha|^2(b_i^2 + b_i^{\dagger 2})$, respectively.

III. "SUPERRADIANT" PHASE

In the thermodynamic limit $N_a \to \infty$, the Dicke model in Eq. (8) displays a second-order phase transition from the normal phase to a superradiant phase, where the $\mathcal{Z}_2$ symmetry [defined by $\{\hat{c}, \hat{\sigma}_x\} \to \{-\hat{c}, -\hat{\sigma}_x\}$] is spontaneously broken and both cavity field and atomic ensemble acquire macroscopic occupations. Such quantum phase transition has been demonstrated theoretically and experimentally [26,38]. The analysis of the critical behavior can be performed using the mean-field solution [26,28,30], which is valid in the thermodynamic limit, and gives the critical coupling [39]

$$\lambda_c = \sqrt{(\omega_0^2 + \kappa^2)\omega_z/4\omega_0}. \tag{10}$$

From the mapping detailed in the previous section, we obtain the corresponding critical point of the optomechanical model:

$$g_c = \sqrt{\frac{(\Delta^2 + \kappa^2)J}{4|\alpha|^2 N\Delta}}, \tag{11}$$

where $N \equiv |b_1|^2 + |b_2|^2$ is the (approximately) conserved total number of phonons. When the optomechanical coupling satisfies $g \leqslant g_c$, the system is in the normal phase with zero occupancy of the displaced cavity mode, $d = 0$, and symmetric phonon numbers, $|b_1|^2 = |b_2|^2$. For $g > g_c$, the $\mathcal{Z}_2$ symmetry is spontaneously broken and the system enters the superradiant phase, which implies a finite expectation value of d and unbalanced phonon occupations, i.e., $\delta N = (|b_1|^2 - |b_2|^2)/2 \neq 0$. The two symmetry-broken states are $|\alpha \mp \bar{d}, \pm\delta\bar{N}\rangle$, with the stationary values

$$\bar{d} = \frac{2g|\alpha|N}{\Delta - i\kappa}\sqrt{1 - \frac{g_c^4}{g^4}}, \tag{12}$$

$$\delta\bar{N} = \frac{N}{2}\sqrt{1 - \frac{g_c^4}{g^4}}. \tag{13}$$

As shown by the dashed lines in Fig. 2, the finite expectation value of Eq. (12) is exact for the effective model and shows good agreement with the stationary value of the full model, in the expected regime of validity. A more detailed comparison of order parameters across the critical coupling is presented in Fig. 3, showing good agreement between analytical expressions and simulations from the original Hamiltonian.

To obtain the above results directly from the mean-field equations (9), without invoking the mapping to the Dicke model, one should consider the ansatz $b_{1,2} \to \beta_{1,2}e^{i\omega t}$. Here $\beta_{1,2}$ are stationary amplitudes and the effective mechanical frequency is given by

$$\omega = 2J\left[1 + \frac{g^2 - g_c^2}{g_c^2}\theta(g - g_c)\right]. \tag{14}$$

Equation (14) reflects the fact that, for $g \leqslant g_c$, the two membranes are coupled oscillators with a symmetric normal mode of frequency $\omega = 2J$ (in the rotating frame). However, the coupling to the cavity should be taken into consideration in the superradiant phase, which modifies the effective frequency of the normal mode. We refer to Appendix B for explicit calculations.

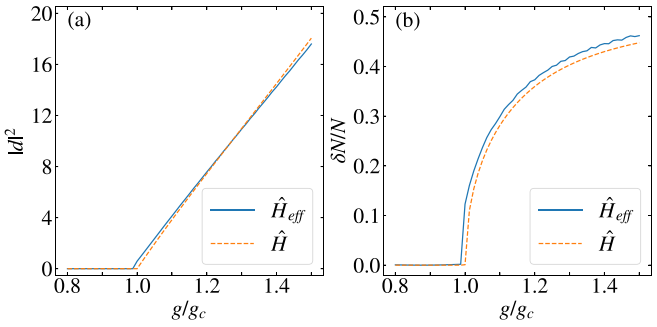

FIG. 3. Dependence on g of two order parameters. (a) Displacement $|d|^2$ of the cavity field. (b) Phonon difference between the two mechanical modes. In each panel, we compare stationary values from the effective Hamiltonian (blue lines) and simulations from the original Hamiltonian (orange dashed lines). We have used the following parameters: $\Delta/J = 20$, $A/J = 2 \times 10^3$, $\kappa/J = 10$, $b_1(0) = b_2(0) = 10$, and $\omega_m/J = 10^4$. The final time of the simulations is $t_f = 80/J$ and $\omega_{1,2}$ are decided by Eq. (5).

Finally, we comment on the role of mechanical dissipation. If the decay of the membranes is considered, the total phonon number is not a conserved quantity but slowly decays with time. Supposing to start from the superradiant phase, and keeping the strength and detuning of the external drive fixed, one finds that the critical coupling g_c slowly grows in time, due to the decrease of N [see Eq. (11)]. During this slow evolution, thanks to the large cavity damping, the system follows adiabatically the broken-symmetry state. Correspondingly, the order parameters of Eqs. (12) and (13) gradually decrease. Finally, when the critical point g_c becomes larger than the fixed coupling strength g, the system recovers the normal phase. From this qualitative description we see that a finite mechanical damping allows one in principle to observe the phase transition in time domain. As the same behavior occurs for the time crystal, we defer a more detailed discussion to Sec. IV E. See, in particular, Fig. 12.

IV. DISCRETE TIME CRYSTAL

The realization of a time crystal in cavity/circuit QED systems, based on a Dicke model with tunable coupling, has been recently proposed in Ref. [16]. The basic idea is to periodically control the dipole interaction and alternate finite coupling and free evolution periods. In an ideal limit, assuming small dissipation and the resonant condition $\omega_z = \omega_0$, the system is in one of two stationary broken-symmetry states for $\lambda > \omega_0/2$. Subsequently, free evolution for a period π/ω_0 accumulates a π phase, which switches the system from one steady state to the other. The repetition of this protocol in time generates a discrete dissipative time crystal, robust to deviations from the ideal limit [16].

However, this idea cannot be applied in a straightforward manner to our optomechanical system. Setting $\lambda = 0$ in Eq. (8) corresponds to $\alpha = 0$, since the bare optomechanical coupling g in Eq. (7) is not easily modified. But turning off the external drive invalidates the resonant condition Eq. (5), on which the mapping from $\hat{H}$ to $\hat{H}_{\rm eff}$ is based. To circumvent this problem, we notice that a free evolution is not necessary, as an equivalent result can be achieved by tuning parameters to the normal phase. Even if the ensuing dynamics is more complex, due to nonlinear features of the (still interacting) model, an approximate π rotation can be realized in this manner. Such incomplete flip is sufficient to establish a discrete time crystal, due to its intrinsic robustness to imperfections. In practice, we consider below a protocol where the critical point g_c is modified through simultaneous adjustments of detuning Δ and drive amplitude A [cf. Eq. (11)]. This allows us to drive the optomechanical system to the normal phase by keeping g and α fixed, thus preserving the mapping to the Dicke model.

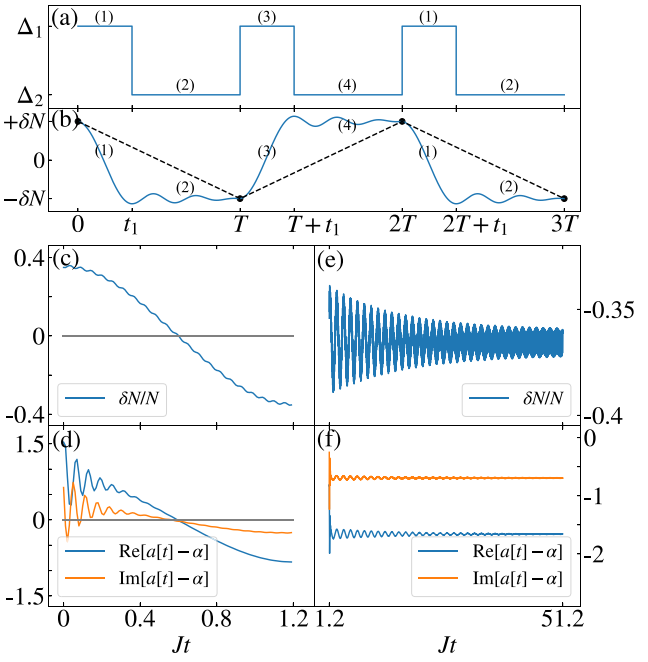

FIG. 4. Discrete time-crystal protocol. The time dependence of detuning, with the corresponding time evolution of δN, are illustrated in panels (a) and (b), respectively. The blue line in panel (b) depicts the continuous-time evolution of the phonon difference and the black dashed line is the stroboscopic dynamics at $t = kT$ ($k = 0, 1, 2, \ldots$). Panels (c) and (d) show the actual time evolution of δN and d during the flipping process (1), obtained from numerical simulations. Panels (e) and (f) show the time evolution during the relaxation process (2). We have used $\Delta_1/J = 100$, $\Delta_2/J = 50$, $A_2/J = 10^4$, $\kappa/J = 10$, $N = 200$, $g = 1.2g_{c,2}$, $\omega_m/J = 10^4$, $t_1 = 1.196/J$, and $t_2 = 100/J$, while A_1 is given by Eq. (15).

A. Period-doubling Floquet dynamics

In Sec. III, we have discussed how the model with two membranes in the cavity exhibits a second-order phase transition in the thermodynamical limit of infinite phonon number, $N \to \infty$, when $g > g_c$. Based on this phase transition, an exact period-doubling Floquet dynamics can be constructed with four basic steps, illustrated in Fig. 4(a). After initializing the system in one of the two symmetry-broken steady states, say $|\alpha - \bar{d}, \delta\bar{N}\rangle$, the protocol reads as follows.

(1) Detuning and drive amplitude are switched to Δ_1 and A_1, respectively, such that $g < g_{c,1}$ and the system is in the normal phase. Importantly, the new values should satisfy $\alpha = A_1/(i\kappa - \Delta_1)$ (i.e., the amplitude of the initialization step

remains unchanged). Now the system undergoes an oscillatory dynamics, shown in panels (c) and (d) of Fig. 4. For a proper evolution time t_1 (the choice of t_1 will be discussed in detail in Sec. IV B), the state is approximately flipped from $|\alpha - \bar{d}, \delta\bar{N}\rangle$ to $|\alpha + \bar{d}, -\delta\bar{N}\rangle$. We note that the effective oscillator should not be in the overdamped regime; otherwise, it will simply relax to $|\alpha, \delta N = 0\rangle$. Even if an oscillatory dynamics takes place, an exact flip is usually not possible.

(2) The detuning is changed to Δ_2 and the drive amplitude to A_2, still satisfying

$$\frac{A_2}{i\kappa - \Delta_2} = \frac{A_1}{i\kappa - \Delta_1}. \tag{15}$$

The values of Δ_2 and A_2 can simply be the initialization values. They are chosen to yield $g > g_{c,2}$ but do not affect the classical amplitude α of the cavity; see Eq. (4). Now the system is in the superradiant phase for a time t_2 (giving the period of the drive $T = t_1 + t_2$) and relaxes towards the nearby steady state, i.e., $|\alpha + \bar{d}, -\delta\bar{N}\rangle$, as illustrated in panels (e) and (f) of Fig. 4 for the mechanical and cavity degrees of freedom, respectively.

(3) Setting $\Delta = \Delta_1$ and $A = A_1$ for a time duration t_1 returns the system to the normal phase, which induces an approximate evolution from $|\alpha + \bar{d}, -\delta\bar{N}\rangle$ to $|\alpha - \bar{d}, \delta\bar{N}\rangle$.

(4) $\Delta = \Delta_2$ and $A = A_2$ for a time duration t_2. At the end of this step, the state is relaxed towards the initial state $|\alpha - \bar{d}, \delta\bar{N}\rangle$.

In summary, the periodic change in detuning and drive amplitude is described by

$$\{\Delta, A\} = \begin{cases} \{\Delta_1, A_1\} & [0, t_1), \\ \{\Delta_2, A_2\} & [t_1, T), \end{cases} \tag{16}$$

where the two pairs are related as in Eq. (15). The system returns to the initial state with period $2T$, thus doubling the period of the control pulse. An example of persistent period-doubling behavior induced by the above control pulse is shown in Fig. 5, through the stroboscopic dynamics of $\delta N/N$ and its discrete Fourier transform:

$$S(\theta) = \frac{1}{n}\sum_{k=1}^{n} \frac{\delta N(k)}{N} \exp(i2\pi k\theta), \tag{17}$$

defined as in Refs. [7,20]. Here, $\delta N(k)$ is the phonon difference between the two membranes at the end of the kth period. Note that the stroboscopic oscillation in Fig. 5(a) is not strictly symmetric around $\delta N = 0$. As the original Hamiltonian is not exactly $\mathcal{Z}_2$ symmetric, the asymmetry reflects small corrections to the effective Dicke model (7).

B. Choice of flipping time

As explained above, each $2T$ operation cycle involves two flipping operations [(1) and (3)], where the steady state $|\alpha \mp \bar{d}, \pm\delta\bar{N}\rangle$ flips to the other steady state $|\alpha \pm \bar{d}, \mp\delta\bar{N}\rangle$. In the presence of decoherence and the always-on interaction g, an analytical expression of the ideal flipping time is not readily available. However, suitable values of t_1 can be found numerically. We find that the choice of the flipping time is rather flexible, because the actual flipping operation has a certain inertia and continues into the relaxation process

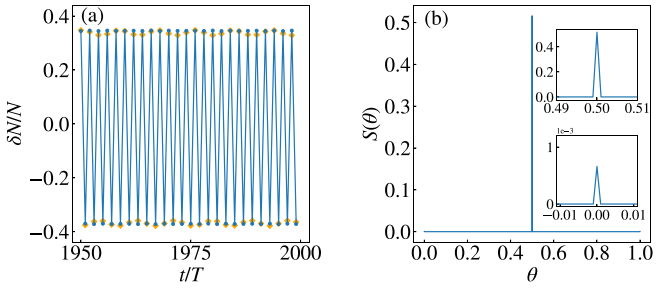

FIG. 5. Persistence of the stroboscopic dynamics. In panel (a) we show the stroboscopic time evolution of $\delta N/N$ in the interval $[1950, 2000] \times T$. In the relaxation phase, we used the same parameters of Figs. 2(b) and 2(c), which give rise to a robust DTC (orange and blue dots, respectively). Instead, we could not realize a DTC with the parameters of Fig. 2(a), due to the difficulty of finding a suitable flipping time t_1. Panel (b) is the discrete Fourier transform of the blue curve of panel (a), computed from Eq. (17) with $n = 2000$. The upper inset of (b) is a zoom-in of the main peak and the lower inset is a zoom-in around $\theta = 0$, showing a small feature induced by the slight asymmetry of the oscillations around $\delta N = 0$. Other parameters: $\Delta_1/J = 40$, $t_1 \approx 1.34/J$, and $t_2 = 20/J$.

even after the system is driven back to the superradiant-phase parameters. To demonstrate this, the evolution in the flipping process (1) (blue lines) is shown in Fig. 6 for different choices of the flipping times t_1. We also continue the time evolution beyond t_1 into the relaxation process (2) (orange lines). One can see that the initial evolution in the relaxation processes (2) is a continuation of the oscillatory dependence of (1). Since an imperfect flipping can be completed during the relaxation phase, see in particular the top panel of Fig. 6, the flipping time t_1 can be chosen in a wide range. In Fig. 7 we mark by a shadowed region (we refer to this as the DTC region) the

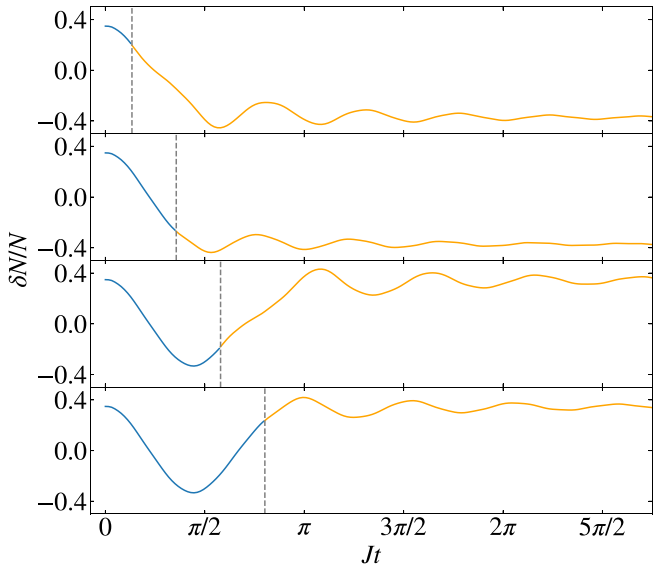

FIG. 6. Time evolution for different choices of the flipping time t_1. The gray dashed lines mark $Jt_1 = \{0.7, 1.4, 2.1, 2.8\}$ (from top to bottom). The time evolution at $t > t_1$ (orange curves) is in the relaxation phase (2). We used $\kappa/J = 10$, $\Delta_1/J = 40$, $\Delta_2/J = 20$, $A_2/J = 2 \times 10^3$, $N = 200$, $g = 1.2g_{c,2}$, and $\omega_m/J = 10^4$.

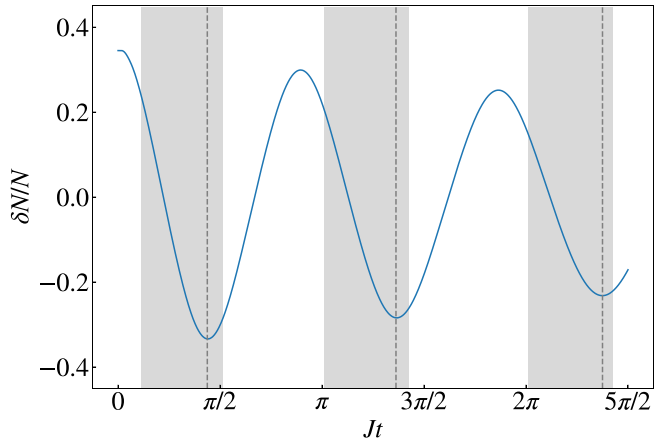

FIG. 7. Flipping times leading to DTC dynamics. The blue line represents the time evolution during the flipping process (1) (without the restriction $t < t_1$). DTC behavior can be obtained by choosing the flipping time t_1 inside the shaded regions. Dashed lines mark the minima of $\delta N/N$, around which the DTC regions are (asymmetrically) located. We used $\kappa/J = 10$, $\Delta_1/J = 40$, $\Delta_2/J = 20$, $A_2/J = 2 \times 10^3$, $N = 200$, $g = 1.2g_{c,2}$, $\omega_m/J = 10^4$, and Jt_2=50.

ranges of t_1, which allow the persistent oscillatory behavior of a time crystal. From the third panel of Fig. 6 we can also see that the continuation of the oscillatory dependence into the relaxation phase can bring back a nearly flipped state to the starting point. For this reason, the DTC regions of Fig. 7 appear at "advanced" times, instead of being centered at the minima of the time evolution (dashed lines).

C. Rigidity of the DTC

In the previous subsection we have shown that, for the proposed control pulse, the optomechanical system exhibits long time oscillations with period doubling. To qualify as a time crystal, this persistent oscillation must be robust against parameter deviations, i.e., it should not occur at a finely tuned point in parameter space. This property is also important for the experimental realization, where imperfections are unavoidable. In this section, we discuss how the DTC phase is affected by variations of different parameters, such as detuning and optomechanical coupling.

Varying Δ_1 and Δ_2, we obtain the phase diagram of DTC order shown in Fig. 8(a). Period doubling occurs in the region marked in red, while in the blue region such behavior is absent. It is evident that period doubling is robust to the imperfection in Δ_1 and Δ_2. In Fig. 8(a) the flipping time t_1 is fixed, but a larger DTC region can be obtained if t_1 is further optimized at each point of the phase diagram; see Fig. 8(b). Here the two black lines indicate the conditions $g_{c,1} = g$ and $g_{c,2} = g$. As explained above, when $g_{c,2} < g < g_{c,1}$ is satisfied, i.e., in region III, the DTC can be realized. However, DTC behavior also occurs in region II, where $g > g_{c,1}$. To understand the persistence of the DTC phase in region II one can introduce an effective potential $V_{\text{eff}}(x)$, where $x = (d + d^*)/\sqrt{2}$ is a quadrature of the cavity (see Appendix C for the derivation). Various profiles of $V_{\text{eff}}(x)$ during the flipping process are shown in Fig. 9, where the red point is the initial position of the cavity and is decided by the previous relaxation

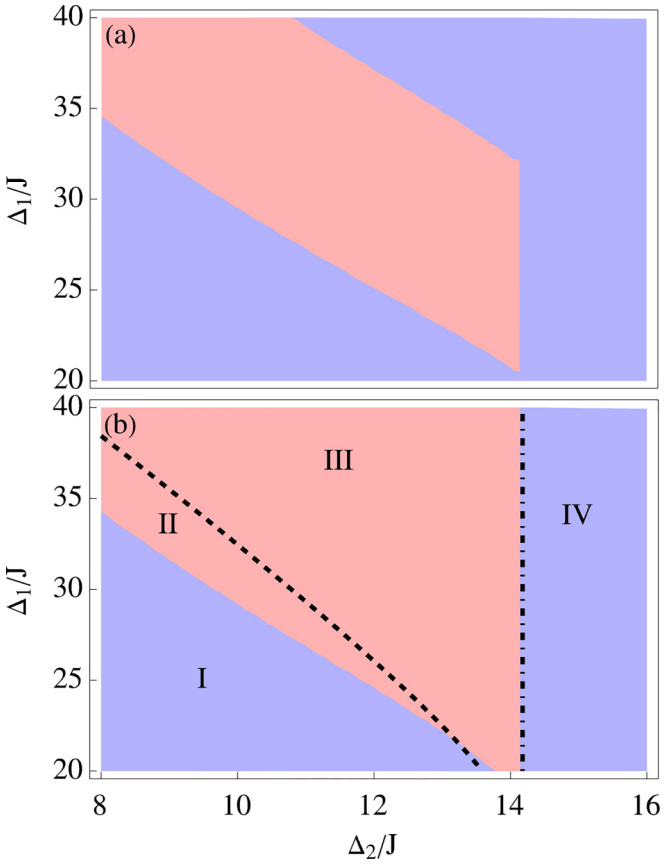

FIG. 8. Phase diagram of DTC order with respect to Δ_1 and Δ_2. The red (blue) region refers to the DTC (non-DTC) phase. The two black lines indicate the conditions $g = g_{c,1}$ (dashed) and $g = g_{c,2}$ (dot-dashed). In panel (a) the flipping time is fixed at $t_1 = 1.90/J$, while in panel (b) t_1 is chosen for each $\Delta_{1/2}$ by the position of the first minimum in the time evolution of δN (see, e.g., Fig. 7). Other parameters are the same for both panels: $\kappa/J = 15$, $A_2/J = 2000$, $g/J = 2 \times 10^{-3}$, $N = 200$, $\omega_m/J = 10^4$, and $Jt_2 = 200$.

process. The effective potentials in I-IV correspond to the four regions of Fig. 8(b). The bottom left panel shows that in region (II), although $g > g_{c,1}$ implies an effective potential with a double-well dependence, the barrier at $x = 0$ is smaller than the initial value of the potential energy and thus does not prevent the flipping process from one steady state $|\alpha - \bar{d}, +\delta\bar{N}\rangle$ to the other steady state $|\alpha + \bar{d}, -\delta\bar{N}\rangle$ from taking place.

Besides being robust to changes in Δ_1 and Δ_2, the period doubling oscillation is also tolerant to deviations from $g_1 = g_2 = g$ (i.e., the condition of equal optomechanical couplings), which is particularly important for the experimental realization. A phase diagram of DTC order with respect to independent optomechanical couplings $g_{1,2}$ is shown in Fig. 10.

D. DTC behavior in the deep quantum regime

While time-crystal order appears in the thermodynamic limit, $N \to \infty$, experimental realizations are certainly limited to a finite excitation number. In principle, at finite N the mean-field approximation is not exact and numerical simulations with the full quantum treatment should be performed. In this regime of finite N, the period-doubling oscillation is only

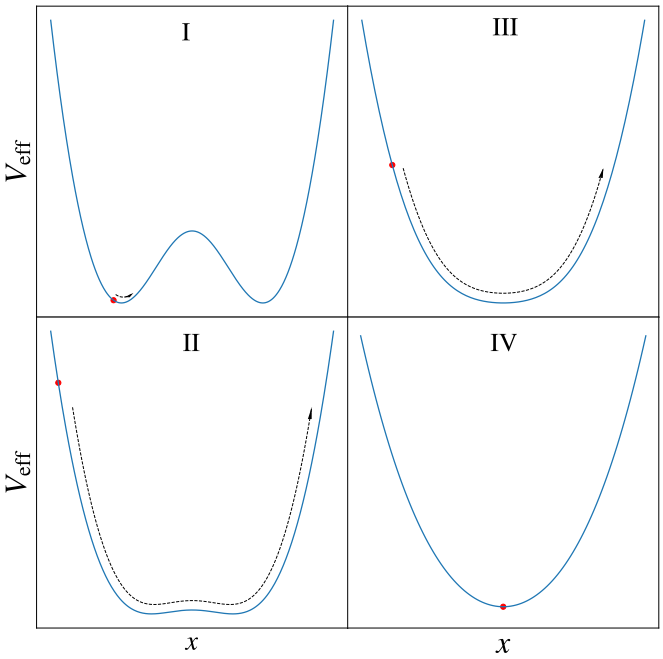

FIG. 9. Schematic plot of the cavity effective potential $V_{\rm eff}(x)$ [cf. Eq. (C3)] during the flipping process, for four possible scenarios. The initial value of x (indicated by a red dot) is decided by the previous relaxation process. Panels I–IV correspond to the four areas in the phase diagram of Fig. 8.

transient. However, their decay time diverges when increasing N. To address these effects, we investigate the few-phonon regime by solving the quantum master equation directly:

$$\frac{d\hat{\rho}}{dt} = -i[\hat{H}_{\rm eff}, \hat{\rho}] + \kappa\left(\hat{d}\hat{\rho}\hat{d}^\dagger - \frac{1}{2}(\hat{d}^\dagger\hat{d}\hat{\rho} + \hat{\rho}\hat{d}^\dagger\hat{d})\right). \quad (18)$$

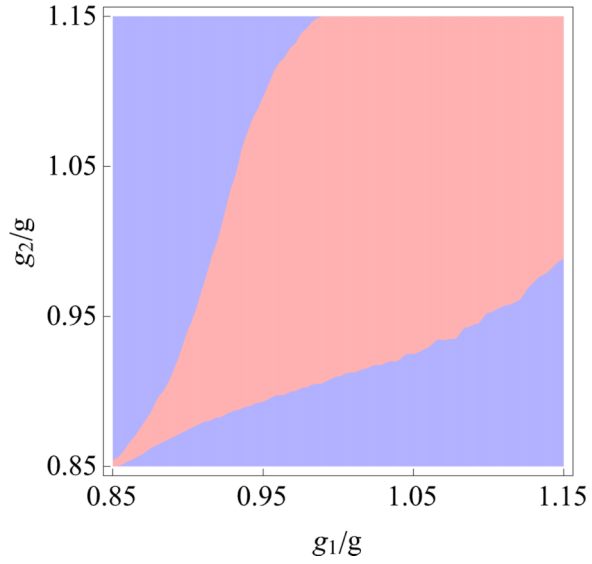

FIG. 10. Phase diagram of DTC order with respect to g_1 and g_2. The red region is the DTC phase. We used $\kappa/J = 10$, $\Delta_1/J = 100$, $\Delta_2/J = 50$, $A_2/J = 10^4$, $N = 200$, $\omega_m/J = 10^4$, and $Jt_2 = 100$. The two optomechanical couplings $g_{1,2}$ are expressed here in terms of $g = 1.2g_{c,2}$ and t_1 is determined at each point of the phase diagram from the first minimum in the oscillations of δN (see, e.g., Fig. 7).

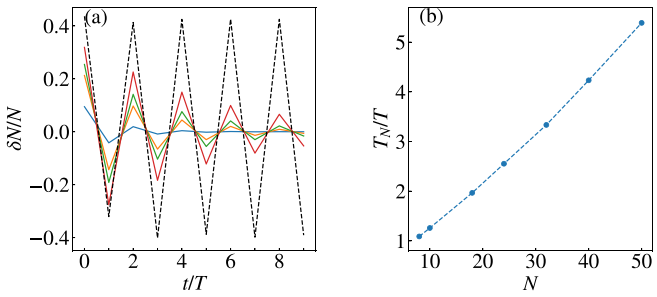

FIG. 11. Period-doubling oscillations in the deep quantum regime. In (a) we show the stroboscopic time evolution of $\delta N/N$ at different values of the (conserved) phonon number N. The dashed black line is the simulation from the original Hamiltonian, obtained by the mean-field approximation. The solid lines are quantum simulations obtained from the master equation (18) using $N = 10, 24, 32, 50$. A larger value of N results in a larger oscillation amplitude. In panel (b) we plot the lifetime T_N (dots), extracted from the simulations of panel (a). The dashed line is a guide for the eye. We used the following parameters: $\kappa/J = 1.2$, $\Delta_1/J = 20$, $\Delta_2/J = 5$, $A_2/J = 300$, $\omega_m/J = 1500$, $g = 1.5g_{c,2}$, $Jt_1 = 5.94$, and $Jt_2 = 5$.

For simplicity, we only perform simulation based on $\hat{H}_{\rm eff}$, expressed as in Eq. (6) through the Schwinger's representation [40]. Oscillations of $\langle\delta\hat{N}/N\rangle = \langle(\hat{b}_1^\dagger\hat{b}_1 - \hat{b}_2^\dagger\hat{b}_2)/2N\rangle$ are displayed in panel (a) of Fig. 11, for different values of the (conserved) phonon number N. As expected, the oscillation period is $2T$. while the amplitude at given N follows an approximate exponential decay $\sim e^{-t/T_N}$. By increasing N, we observe both a general increase of amplitude, bringing the oscillations closer to the mean-field result (dashed curve), as well as a longer decay time T_N.

The growth of T_N with N, shown in Fig. 11(b), is consistent with a robust DTC order in the thermodynamic limit. The dependence is slightly faster than linear in the available range of N, but the precise functional form is difficult to ascertain. If larger values of N were accessible, T_N might show the same type of weak exponential growth discussed in Ref. [16]. While it is numerically difficult to extend the simulations to larger N, we note that the total number of phonons is naturally large in our optomechanical model, which validates the thermodynamic limit and justifies the mean-field description adopted in the rest of the article. Instead, in Ref. [16] the number of artificial atoms is typically of order $O(1)$.

E. Mechanical dissipation

So far all our discussions have assumed negligible mechanical dissipation. Then, within the regime of validity of the effective Dicke model Eq. (7), the initial phonon number N is conserved. Instead, if the decay of the membrane is considered the total phonon number becomes time dependent and follows the approximate exponential decay $N(t) \approx N_0 \exp[-2\gamma t]$ (assuming equal decay rates of the two mechanical modes, $\gamma_1 = \gamma_2 = \gamma$). Consequently, the two critical couplings $g_{c,i}(t)$ (with $i = 1, 2$) increase with time. The value of $g_{c,2}(t)$ is most important here for the stability of DTC order and Eq. (11)

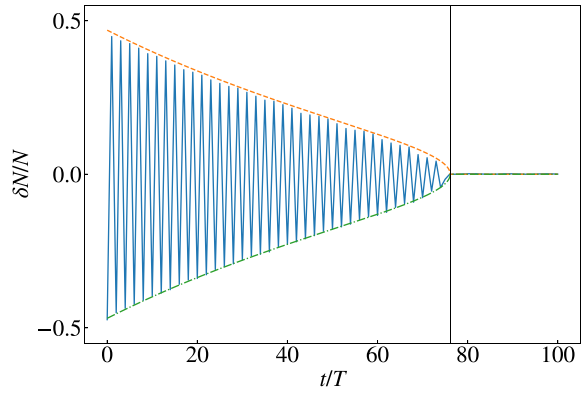

FIG. 12. Evolution of the DTC order parameter $\delta N/N$ after including the decay of the mechanical modes. The blue curve is the numerical evolution, obtained from the mean-field equations of the full model; see Eq. (1). The dashed and dot-dashed curves are from Eq. (21). We have used the following parameters: $\Delta_1/J = 80$, $\Delta_2/J = 20$, $A_2/J = 2000$, $\kappa/J = 10$, $\gamma/J = 10^{-3}$, $\omega_m/J = 10^4$, $Jt_1 = 0.97$, $Jt_2 = 6$, and $g = 1.7g_{c,2}(0)$, where the critical coupling $g_{c,2}(0)$ is computed from Eq. (11) using $N = 200$ (the initial number of phonons). The value of A_1 is determined by Eq. (15).

gives

$$g_{c,2}(t) = \sqrt{\frac{(\Delta_2^2 + \kappa^2)J}{4\Delta_2|\alpha|^2 N_0}}\exp[\gamma t]. \tag{19}$$

As seen in Fig. 8, DTC order only occurs for $g > g_{c,2}$. Otherwise, the relaxation phase drives the system to the normal state and the DTC order cannot persist. Imposing $g_{c,2}(t) = g$, the lifetime T_0 of the DTC is found as follows:

$$T_0 = \frac{1}{\gamma}\ln\left[\frac{g}{g_{c,2}(0)}\right]. \tag{20}$$

For $t < T_0$, the amplitudes of the period-doubling oscillations decay as

$$\bar{d}(t) = \frac{2g|\alpha|N_0\exp[-2\gamma t]}{\Delta_2 - i\kappa}\sqrt{1 - \frac{g_{c,2}^4(t)}{g^4}},$$
$$\delta\bar{N}(t) = \frac{N_0\exp[-2\gamma t]}{2}\sqrt{1 - \frac{g_{c,2}^4(t)}{g^4}}, \tag{21}$$

while for $t \geqslant T_0$ the period-doubling oscillations have disappeared. An example of DTC dynamics with finite mechanical damping is shown in Fig. 12, finding excellent agreement with Eqs. (20) and (21).

F. Experimental feasibility

A main motivation for our setup has been the large difference in relaxation rates between the cavity and the mechanical modes. In a wide range of optomechanics setups, the decay rate of the mechanical mode is $\gamma \sim (10^{-4}$–$10^{-7})\,\omega_m$, which can be 10^5–10^6 times smaller than κ (see, e.g., Table II of Ref. [23]). This makes it desirable to develop a mapping in which the low-dissipation mechanical modes correspond to the atomic ensemble of the Dicke model.

Throughout the paper, we have used values of the couplings g and J, which are generally compatible with existing optomechanical setups. In particular, a large second-order interaction with $g/2\pi = 245$ Hz has been realized in an optomechanical crystal [41] (in that case $\omega_m/2\pi \simeq 9$ MHz, giving $g \sim 3 \times 10^{-5}\,\omega_m$). Furthermore, reported values of the structural coupling parameter J are typically $J \sim 10^{-3}\,\omega_m$, while reaching up to $J \sim 10^{-2}\,\omega_m$ [33,35,36]. In our simulations we assumed values well within, or much smaller than, these typical scales. For example, we take $2J = (10^{-2}$–$10^{-4})\,\omega_m$ and $g \simeq (10^{-5}$–$10^{-7})\,\omega_m$ in Fig. 2. The parameters of Figs. 2(b) and 2(c) were also used to compute the DTC dynamics of Fig. 5.

On the other hand, we find that the RWA conditions $\omega_m \gg JN, g|\alpha|^2 N$ (under which the mapping to the Dicke model becomes accurate) can represent a significant restriction. They are satisfied by simply assuming a sufficiently large value of the mechanical frequency ω_m. However, in this regime it might be more challenging to realize a large second-order optomechanical coupling g. Furthermore, due to the large value of ω_m, our simulations were performed deep in the resolved sideband regime. The most favorable value considered in Figs. 2 and 5 is $\kappa \simeq 0.005\,\omega_m$, which is not too far from experimental realizations [23], but still not in the achievable range.

To address this issue, we extend in Fig. 13(a) the calculations of DTC dynamics of Fig. 5 by considering progressively larger values of κ/ω_m. We observe a significant decay of the DTC oscillations which, for the case with largest cavity damping ($\kappa = 0.04\,\omega_m$), terminate after about 500 periods. This decay of the oscillation amplitude is qualitatively similar to the effect of a finite mechanical damping. In fact, we show in Fig. 13(b) that here the DTC protocol induces a decay of the total photon number N (even if $\gamma = 0$). We recall that for an accurate mapping the total phonon number N is approximately conserved. Thus the observed decay reflects progressively larger violations of the RWA condition. Furthermore, it can be seen in Fig. 13(a) that the center of the DTC oscillations gets gradually displaced from $\delta N = 0$. This feature, noted already, is also due to the imperfect mapping.

Despite these obvious imperfections, the DTC oscillations of Fig. 13 are long-lived. As shown by the black curve of Fig. 13(b), the decay induced by the natural damping of a high-quality mechanical mode occurs on a much faster timescale and thus would completely dominate over the decay observed in Fig. 13(a). If mechanical damping were included, the DTC oscillations would be limited to at most ~100 periods, similar to Fig. 12. These discussions suggest that that, in realistic systems, it is meaningful to explore the DTC phase beyond the regime of strict validity of our mapping. This can relax the restrictions on parameters and facilitate the realization of our proposed setup.

V. CONCLUSION

In this work we have proposed a scheme for the realization of a superradiant-type quantum phase transition in a two membranes in the middle optomechanical system. We identify a regime in which the system can be accurately mapped to the Dicke model and exhibits Z_2 symmetry breaking in the thermodynamic limit. By modulating the drive amplitude and

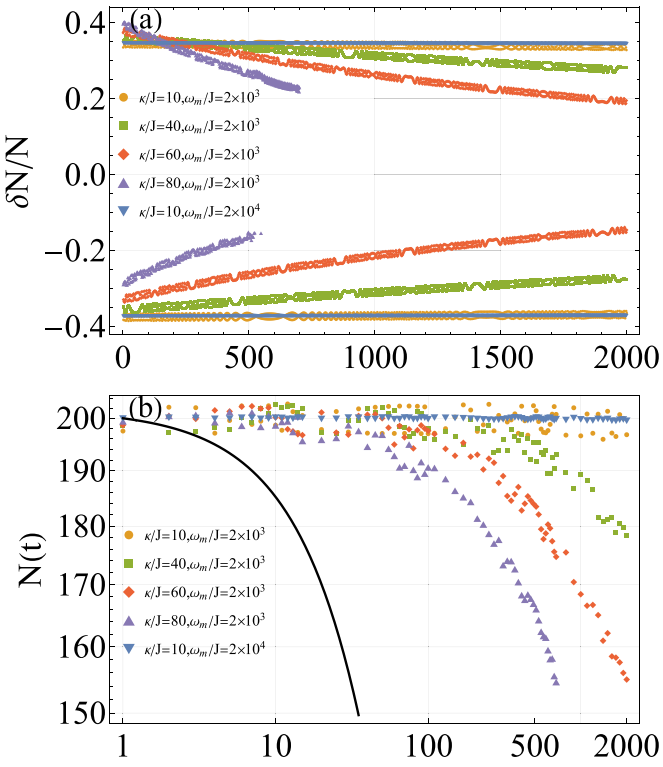

FIG. 13. Period-doubling oscillations with progressively larger values of κ. Panel (a) shows the amplitude of the stroboscopic dynamics. For reference, we plot the same oscillations of Fig. 5(a) where $\kappa/\omega_m = 0.0005$ and 0.005 (blue and yellow symbols, respectively), showing negligible decay. The other curves are for $\kappa/\omega_m = 0.02$ (green squares), 0.04 (red diamonds), and 0.04 (violet triangles). In these three cases we used $\Delta_1/J = 10J$, while all other parameters are as in Fig. 5. The symbols of panel (b) show the corresponding evolution of the phonon number. The solid black line is $N(t) = N_0 \exp[-2\gamma t]$, using $\gamma = 10^{-7}\,\omega_m$.

detuning in a periodic way, making the system cross the normal/superradiant critical point, one can realize a discrete time crystal order with period doubling. We show that such period doubling is robust to parameter deviations and persists in the thermodynamic limit. We also discussed how the realization of the present setup, while challenging, is broadly compatible with currently available optomechanical technology.

ACKNOWLEDGMENTS

Y.D.W. acknowledges support from NSFC (Grant No. 12275331) and the Penghuanwu Innovative Research Center (Grant No. 12047503). S.C. acknowledges support from the National Science Association Funds (Grant No. U2230402), and NSFC (Grants No. 11974040 and No. 12150610464). Y.D.W. and S.C. acknowledge support from the Innovation Program for Quantum Science and Technology (Grant No. 2021ZD0301602).

APPENDIX A: FEASIBILITY OF THE MODEL

In this Appendix, we demonstrate an implementation of the model. The specific example we consider is a Fabry-Pérot cavity with two membranes in the middle. As indicated in Fig. 1, the laser axis is along the x direction, with the two end mirrors at positions $x = \pm L$. In analogy to Refs. [42–44], we model the membranes as dielectric "bumps" with transmission coefficient $\mathcal{T}$ and apply suitable boundary conditions at the end mirrors and at the positions of the two membranes. A transcendental equation can be obtained

$$\sin(2kL + 2\varphi) + \sin[2kL + 2k(x_1 - x_2)]\sin^2\varphi - 2\sin\varphi\cos[k(x_1 - x_2) - \varphi]\cos[k(x_1 + x_2)] = 0, \tag{A1}$$

where k is the wave number of the optical mode and $\varphi = \arccos\sqrt{\mathcal{T}}$. We now impose the condition of vanishing first-order optomechanical couplings and require that the second-order couplings have the same form of Eq. (2):

$$\frac{\partial k}{\partial x_1} = \frac{\partial k}{\partial x_2} = \frac{\partial^2 k}{\partial x_1 \partial x_2} = 0, \quad \frac{\partial^2 k}{\partial x_1^2} = -\frac{\partial^2 k}{\partial x_2^2}. \tag{A2}$$

By evaluating the first- and second-order derivatives of Eq. (A1), we rewrite Eq. (A2) as

$$\begin{aligned} &\sin(2kx_1 - \varphi) + \cos[2k(L + x_1 - x_2)]\sin\varphi = 0, \\ &\sin(2kx_2 + \varphi) - \cos[2k(L + x_1 - x_2)]\sin\varphi = 0, \\ &\sin[2k(L + x_1 - x_2)] = 0, \\ &\cos(2kx_1 - \varphi) = -\cos(2kx_2 + \varphi). \end{aligned} \tag{A3}$$

A solution of Eq. (A3) is

$$k = \frac{(2m_0 + 1)\pi}{2L} - \frac{\varphi}{L}, \quad x_1^{(0)} = \frac{m_1\pi}{k}, \quad x_2^{(0)} = \frac{m_2\pi + \pi/2 - \varphi}{k}, \tag{A4}$$

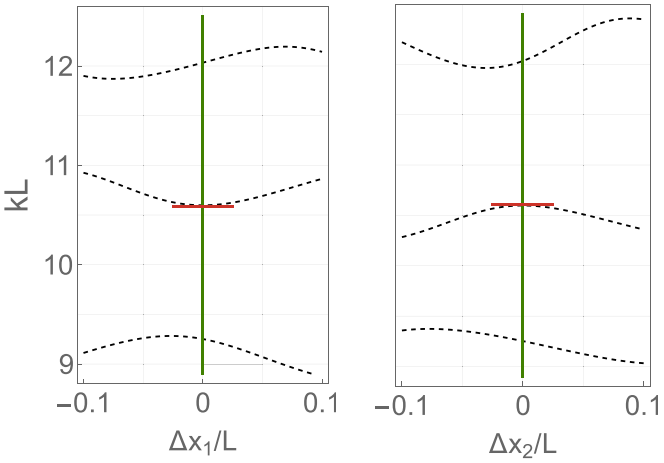

FIG. 14. Optical spectrum of the two-membrane cavity, close to the condition determined by Eq. (A4). Here we choose $m_0 = 7$, $m_1 = -1$, $m_2 = 1$, and $\mathcal{T} = 0.85$, giving $x_1^{(0)}/L \simeq -0.296$ and $x_2^{(0)}/L \simeq 0.407$. The left (right) panel shows the optical spectrum as a function of Δx_1 (Δx_2), while setting $\Delta x_2 = 0$ ($\Delta x_1 = 0$). For the middle mode, the vanishing derivatives (indicated by red lines) imply zero first-order optomechanical couplings. The opposite curvatures with respect to changes in Δx_1 and Δx_2 correspond to second-order optomechanical couplings with opposite sign.

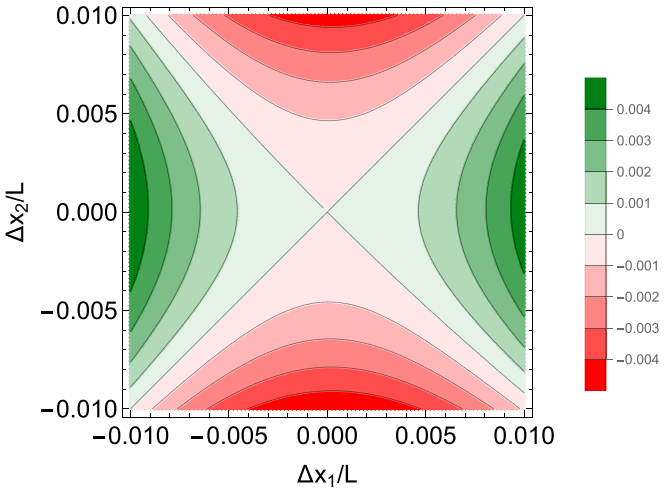

FIG. 15. Optical spectrum for the middle mode of Fig. 14. More precisely, we plot $L\Delta k = L[k(x_1, x_2) - k(x_1^{(0)}, x_2^{(0)})]$ as a function of Δx_1, Δx_2. As expected, Δk is approximately $\propto \Delta x_1^2 - \Delta x_2^2$ for small values of $\Delta x_{1,2}$.

where m_0, m_1, m_2 are integers. For specific parameters, the dependence of the optical spectrum as a function of the displacements $\Delta x_i = x_i - x_i^{(0)}$ $(i = 1, 2)$ is illustrated in Figs. 14 and 15, showing that one of the eigenmodes follows the expected behavior.

APPENDIX B: PHASE TRANSITION FROM THE MEAN-FIELD EQUATIONS

The effective Hamiltonian is shown in Eq. (6) and the corresponding mean-field equations of motion are presented in Eq. (9). By substituting $b_{1,2} \to \beta_{1,2} e^{i\omega t}$, where $\beta_{1,2}$ are time-independent amplitudes, we get

$$\begin{aligned} \omega\beta_1 &= -2g|\alpha|(d + d^*)\beta_1 + 2J\beta_2, \\ \omega\beta_2 &= 2g|\alpha|(d + d^*)\beta_2 + 2J\beta_1, \end{aligned} \tag{B1}$$

which can only have a nontrivial solution for

$$\omega = \pm\sqrt{4g^2|\alpha|^2(d + d^*)^2 + 4J^2}. \tag{B2}$$

This equation describes how the unperturbed frequencies $\pm 2J$ of the normal modes are modified by a finite expectation value of the cavity field. In terms of ω and d, and by using the conserved total phonon number $N = |b_1|^2 + |b_2|^2$, we find

$$|\beta_1|^2 = \frac{4J^2 N}{4J^2 + [2g|\alpha|(d + d^*) + \omega]^2},$$

$$|\beta_2|^2 = \frac{N[2g|\alpha|(d + d^*) + \omega]^2}{4J^2 + [2g|\alpha|(d + d^*) + \omega]^2}. \tag{B3}$$

Assuming a stationary d, the mean-field equations also give $d = 2g|\alpha|(|\beta_2|^2 - |\beta_1|^2)/(\Delta - i\kappa)$, implying

$$(\Delta^2 + \kappa^2)(d + d^*) = \pm\frac{4g^2|\alpha|^2\Delta N(d + d^*)}{\sqrt{J^2 + g^2(d + d^*)^2|\alpha|^2}}, \tag{B4}$$

where the $\pm$ sign corresponds to Eq. (B2) and, assuming $d \neq 0$, must be chosen in accordance with the sign of Δ. For $g > g_c$, the above condition has the following nontrivial solution:

$$(d + d^*)^2 = \frac{16g^2|\alpha|^2\Delta N^2}{(\Delta^2 + \kappa^2)^2}\left(1 - \frac{g_c^4}{g^4}\right), \tag{B5}$$

which is in agreement with Eqs. (11) and (12). Substituting Eq. (B5) in the expression (B2) for ω, we find the effective frequency (14) given in the main text. Finally, we can recover Eq. (13) using Eq. (B3).

APPENDIX C: EFFECTIVE POTENTIAL OF THE CAVITY

In this appendix, we introduce an effective potential $V_{\text{eff}}(x)$ of the cavity. We first rewrite the mean-field equation of motion for the cavity, see Eq. (9), in terms of the quadrature variables as follows: We have

$$\begin{aligned} \frac{dx}{dt} &= \Delta p - \kappa x, \\ \frac{dp}{dt} &= -\Delta x - 2\sqrt{2}g|\alpha|(|b_1|^2 - |b_2|^2) - \kappa p, \end{aligned} \tag{C1}$$

where $x = (d^* + d)/\sqrt{2}$ and $p = i(d^* - d)/\sqrt{2}$. It is then simple to derive the following equation of motion for x:

$$\frac{d^2x}{dt^2} = -\frac{dV_{\text{eff}}(x)}{dx} - 2\kappa\frac{dx}{dt}, \tag{C2}$$

where $\frac{dV_{\text{eff}}(x)}{dx} = (\Delta^2 + \kappa^2)x + 2\sqrt{2}g|\alpha|\Delta(|b_1|^2 - |b_2|^2)$. With the values of $|b_{1,2}|^2$ given by Eqs. (B3) and (B2), the following explicit form of the effective potential is found:

$$V_{\text{eff}}(x) = \frac{1}{2}(\Delta^2 + \kappa^2)x^2 + 2\Delta N\sqrt{J^2 + 2|\alpha|^2 g^2 x^2}. \tag{C3}$$

The critical coupling g associated with $V_{\text{eff}}(x)$ coincides with Eq. (11) and in the broken-symmetry phase the minima of $V_{\text{eff}}(x)$ agree with Eq. (12).

[1] F. Wilczek, Quantum time crystals, Phys. Rev. Lett. **109**, 160401 (2012).
[2] P. Bruno, Comment on "quantum time crystals", Phys. Rev. Lett. **110**, 118901 (2013).
[3] P. Bruno, Impossibility of spontaneously rotating time crystals: A no-go theorem, Phys. Rev. Lett. **111**, 070402 (2013).
[4] H. Watanabe and M. Oshikawa, Absence of quantum time crystals, Phys. Rev. Lett. **114**, 251603 (2015).
[5] V. Khemani, A. Lazarides, R. Moessner, and S. L. Sondhi, Phase structure of driven quantum systems, Phys. Rev. Lett. **116**, 250401 (2016).
[6] D. V. Else, B. Bauer, and C. Nayak, Floquet time crystals, Phys. Rev. Lett. **117**, 090402 (2016).
[7] N. Y. Yao, A. C. Potter, I.-D. Potirniche, and A. Vishwanath, Discrete time crystals: Rigidity, criticality, and realizations, Phys. Rev. Lett. **118**, 030401 (2017).

[8] D. V. Else, C. Monroe, C. Nayak, and N. Y. Yao, Discrete time crystals, Annu. Rev. Condens. Matter Phys. **11**, 467 (2020).

[9] A. Russomanno, F. Iemini, M. Dalmonte, and R. Fazio, Floquet time crystal in the Lipkin-Meshkov-Glick model, Phys. Rev. B **95**, 214307 (2017).

[10] J. Zhang, P. W. Hess, A. Kyprianidis, P. Becker, A. Lee, J. Smith, G. Pagano, I. D. Potirniche, A. C. Potter, A. Vishwanath, N. Y. Yao, and C. Monroe, Observation of a discrete time crystal, Nature (London) **543**, 217 (2017).

[11] S. Choi, J. Choi, R. Landig, G. Kucsko, H. Zhou, J. Isoya, F. Jelezko, S. Onoda, H. Sumiya, V. Khemani, C. von Keyserlingk, N. Y. Yao, E. Demler, and M. D. Lukin, Observation of discrete time-crystalline order in a disordered dipolar many-body system, Nature (London) **543**, 221 (2017).

[12] S. Autti, V. B. Eltsov, and G. E. Volovik, Observation of a time quasicrystal and its transition to a superfluid time crystal, Phys. Rev. Lett. **120**, 215301 (2018).

[13] S. Pal, N. Nishad, T. S. Mahesh, and G. J. Sreejith, Temporal order in periodically driven spins in star-shaped clusters, Phys. Rev. Lett. **120**, 180602 (2018).

[14] J. Rovny, R. L. Blum, and S. E. Barrett, Observation of discrete-time-crystal signatures in an ordered dipolar many-body system, Phys. Rev. Lett. **120**, 180603 (2018).

[15] H. Keßler, P. Kongkhambut, C. Georges, L. Mathey, J. G. Cosme, and A. Hemmerich, Observation of a dissipative time crystal, Phys. Rev. Lett. **127**, 043602 (2021).

[16] Z. Gong, R. Hamazaki, and M. Ueda, Discrete time-crystalline order in cavity and circuit qed systems, Phys. Rev. Lett. **120**, 040404 (2018).

[17] B. Zhu, J. Marino, N. Y. Yao, M. D. Lukin, and E. A. Demler, Dicke time crystals in driven-dissipative quantum many-body systems, New J. Phys. **21**, 073028 (2019).

[18] R. J. L. Tuquero, J. Skulte, L. Mathey, and J. G. Cosme, Dissipative time crystal in an atom-cavity system: Influence of trap and competing interactions, Phys. Rev. A **105**, 043311 (2022).

[19] J. G. Cosme, J. Skulte, and L. Mathey, Bridging closed and dissipative discrete time crystals in spin systems with infinite-range interactions, Phys. Rev. B **108**, 024302 (2023).

[20] C. H. Fan, D. Rossini, H.-X. Zhang, J.-H. Wu, M. Artoni, and G. C. La Rocca, Discrete time crystal in a finite chain of rydberg atoms without disorder, Phys. Rev. A **101**, 013417 (2020).

[21] P. Liang, R. Fazio, and S. Chesi, Time crystals in the driven transverse field Ising model under quasiperiodic modulation, New J. Phys. **22**, 125001 (2020).

[22] K. Giergiel, A. Dauphin, M. Lewenstein, J. Zakrzewski, and K. Sacha, Topological time crystals, New J. Phys. **21**, 052003 (2019).

[23] M. Aspelmeyer, T. J. Kippenberg, and F. Marquardt, Cavity optomechanics, Rev. Mod. Phys. **86**, 1391 (2014).

[24] S. Barzanjeh, A. Xuereb, S. Gröblacher, M. Paternostro, C. A. Regal, and E. M. Weig, Optomechanics for quantum technologies, Nat. Phys. **18**, 15 (2022).

[25] J. Mumford, D. O'Dell, and J. Larson, Dicke-type phase transition in a multimode optomechanical system, Ann. Phys. (Leipzig) **527**, 115 (2015).

[26] F. Dimer, B. Estienne, A. S. Parkins, and H. J. Carmichael, Proposed realization of the Dicke-model quantum phase transition in an optical cavity QED system, Phys. Rev. A **75**, 013804 (2007).

[27] D. Nagy, G. Kónya, G. Szirmai, and P. Domokos, Dicke-model phase transition in the quantum motion of a Bose-Einstein condensate in an optical cavity, Phys. Rev. Lett. **104**, 130401 (2010).

[28] P. Kirton, M. M. Roses, J. Keeling, and E. G. Dalla Torre, Introduction to the Dicke model: From equilibrium to nonequilibrium, and vice versa, Adv. Quantum Technol. **2**, 1970013 (2019).

[29] J. Gelhausen, M. Buchhold, and P. Strack, Many-body quantum optics with decaying atomic spin states: (γ, κ) Dicke model, Phys. Rev. A **95**, 063824 (2017).

[30] P. Kirton and J. Keeling, Suppressing and restoring the Dicke superradiance transition by dephasing and decay, Phys. Rev. Lett. **118**, 123602 (2017).

[31] F. Reiter, T. L. Nguyen, J. P. Home, and S. F. Yelin, Cooperative breakdown of the oscillator blockade in the Dicke model, Phys. Rev. Lett. **125**, 233602 (2020).

[32] M. Spletzer, A. Raman, A. Q. Wu, X. Xu, and R. Reifenberger, Ultrasensitive mass sensing using mode localization in coupled microcantilevers, Appl. Phys. Lett. **88**, 254102 (2006).

[33] R. B. Karabalin, M. C. Cross, and M. L. Roukes, Nonlinear dynamics and chaos in two coupled nanomechanical resonators, Phys. Rev. B **79**, 165309 (2009).

[34] H. Yabuno, Y. Seo, and M. Kuroda, Self-excited coupled cantilevers for mass sensing in viscous measurement environments, Appl. Phys. Lett. **103**, 063104 (2013).

[35] H. Okamoto, A. Gourgout, C.-Y. Chang, K. Onomitsu, I. Mahboob, E. Y. Chang, and H. Yamaguchi, Coherent phonon manipulation in coupled mechanical resonators, Nat. Phys. **9**, 480 (2013).

[36] H. Fu, Z.-C. Gong, L.-P. Yang, T.-H. Mao, C.-P. Sun, S. Yi, Y. Li, and G.-Y. Cao, Coherent optomechanical switch for motion transduction based on dynamically localized mechanical modes, Phys. Rev. Appl. **9**, 054024 (2018).

[37] J. D. Thompson, B. M. Zwickl, A. M. Jayich, F. Marquardt, S. M. Girvin, and J. G. E. Harris, Strong dispersive coupling of a high-finesse cavity to a micromechanical membrane, Nature (London) **452**, 72 (2008).

[38] Z. Zhiqiang, C. H. Lee, R. Kumar, K. J. Arnold, S. J. Masson, A. S. Parkins, and M. D. Barrett, Nonequilibrium phase transition in a spin-1 Dicke model, Optica **4**, 424 (2017).

[39] C. Emary and T. Brandes, Chaos and the quantum phase transition in the Dicke model, Phys. Rev. E **67**, 066203 (2003).

[40] J. Johansson, P. Nation, and F. Nori, QuTiP: An open-source python framework for the dynamics of open quantum systems, Comput. Phys. Commun. **183**, 1760 (2012).

[41] T. K. Paraïso, M. Kalaee, L. Zang, H. Pfeifer, F. Marquardt, and O. Painter, Position-squared coupling in a tunable photonic crystal optomechanical cavity, Phys. Rev. X **5**, 041024 (2015).

[42] M. B. Spencer and W. E. Lamb, Theory of two coupled lasers, Phys. Rev. A **5**, 893 (1972).

[43] M. Bhattacharya and P. Meystre, Multiple membrane cavity optomechanics, Phys. Rev. A **78**, 041801(R) (2008).

[44] M. J. Hartmann and M. B. Plenio, Steady state entanglement in the mechanical vibrations of two dielectric membranes, Phys. Rev. Lett. **101**, 200503 (2008).